Macroscopic materials assembled from nanoparticle superlattices

https://doi.org/10.1038/s41586-021-03355-z

Received: 31 July 2020

Accepted: 12 February 2021

Published online: 24 March 2021

Check for updates

Peter J. Santos[1,2], Paul A. Gabrys[1,2], Leonardo Z. Zornberg[1], Margaret S. Lee[1] & Robert J. Macfarlane[1]✉

Nanoparticle assembly has been proposed as an ideal means to program the hierarchical organization of a material by using a selection of nanoscale components to build the entire material from the bottom up. Multiscale structural control is highly desirable because chemical composition, nanoscale ordering, microstructure and macroscopic form all affect physical properties[1,2]. However, the chemical interactions that typically dictate nanoparticle ordering[3–5] do not inherently provide any means to manipulate structure at larger length scales[6–9]. Nanoparticle-based materials development therefore requires processing strategies to tailor micro- and macrostructure without sacrificing their self-assembled nanoscale arrangements. Here we demonstrate methods to rapidly assemble gram-scale quantities of faceted nanoparticle superlattice crystallites that can be further shaped into macroscopic objects in a manner analogous to the sintering of bulk solids. The key advance of this method is that the chemical interactions that govern nanoparticle assembly remain active during the subsequent processing steps, which enables the local nanoscale ordering of the particles to be preserved as the macroscopic materials are formed. The nano- and microstructure of the bulk solids can be tuned as a function of the size, chemical makeup and crystallographic symmetry of the superlattice crystallites, and the micro- and macrostructures can be controlled via subsequent processing steps. This work therefore provides a versatile method to simultaneously control structural organization across the molecular to macroscopic length scales.

Nanoparticle assembly is typically governed by chemical interactions between small-molecule ligands grafted to the surface of each particle[3,4], and previous efforts have used different ligands to create one-dimensional ribbons[10,11], thin films[12–14] and micrometre-scale single crystals[15–21] with precise nanoscale organization of individual particles. However, to use these assemblies as components of bulk macroscopic solids, it is also necessary to control material organization at larger length scales. Microstructure and macroscopic form remain underexplored design parameters, and the development of processing techniques that can coalesce individual self-assembled structures into macroscopic solids would be an important step in the development of nanoparticle-based bulk solids with complete structure control at all size regimes.

The nanocomposite tecton (NCT)[22] is a recently developed building block that is well-suited for producing such hierarchical materials, as it consists of inherently scalable components and uses dynamic binding interactions to dictate how nanoparticles arrange themselves into ordered arrays (Fig. 1). Each NCT consists of an inorganic nanoparticle core covered with a polymer brush, in which every polymer chain terminates in a supramolecular binding group (Fig. 1b). Upon mixing solvent-dispersed NCTs with complementary binding groups, supramolecular interactions guide the assembly of particles into larger structures. Because the supramolecular interactions that link NCTs together are dynamic, cooling a set of NCTs through their dissociation temperature (the melting temperature, T_m; Supplementary Fig. 28) enables them to organize into ordered superlattices—for example, body-centred cubic (bcc) arrays[23] (Fig. 1c). However, previous attempts to remove the lattices from the assembly solvent caused the lattices to disorder, as the polymer chains rapidly contract during drying (Supplementary Fig. 3). Thus, the formation of free-standing macroscopic solids from these NCT assemblies first requires methods to stabilize them against the loss of ordering during solvent removal[24,25].

Stabilizing colloidal assemblies as solids

Because the assembly process occurs in a solvent that swells the NCT polymer brush, we proposed that the lattices could be stabilized against collapse of the polymer brushes by gradually introducing a non-solvent that has an unfavourable interaction energy with the polymer; interactions with this non-solvent would cause the chains to adopt denser conformations and shrink the lattice[26]. A model NCT system was therefore developed using previously established chemistry[27]: 15.4-nm gold nanoparticle cores (AuNPs), 14-kDa polystyrene polymer brushes, and diaminopyridine–thymine (DAP–Thy) hydrogen-bonding pairs to link the NCTs (Supplementary Figs. 1, 2, Supplementary Tables 1, 2). This NCT is readily dispersed in toluene,

[1]Department of Materials Science and Engineering, Massachusetts Institute of Technology, Cambridge, MA, USA. [2]These authors contributed equally: Peter J. Santos, Paul A. Gabrys. ✉e-mail: rmacfarl@mit.edu

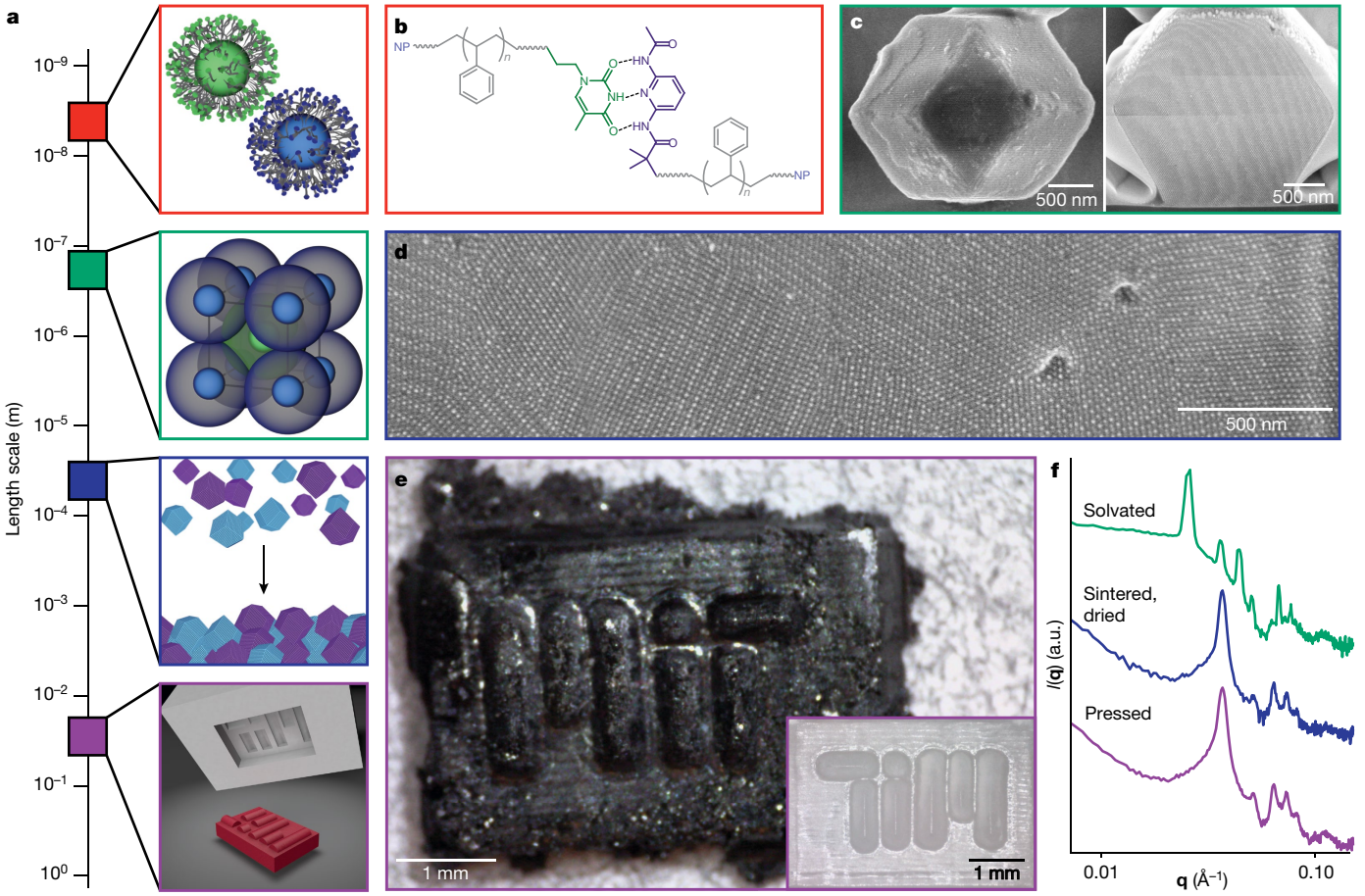

Fig. 1 | NCTs can be processed into bulk solids with simultaneous structural control across seven orders of magnitude on the length scale. **a**, Supramolecular interactions assemble nanoparticles (red) into ordered superlattices (green), which form micrometre-sized crystallites (blue); these crystallites are 'sintered' via centrifugation into a macroscopic material (purple), which is dried and pressed with a mould. **b**, The chemical structure of the NCT ligand coating: a polymer brush that terminates in one-half of a supramolecular binding group, where hydrogen-bonding interactions enable NCT–NCT bonds to be formed. NP, nanoparticle. **c**, SEM micrographs of the surface morphology (left) and cross-section (right) of an NCT crystallite. **d**, SEM micrograph of a cross-section of the sintered NCT solid. **e**, Optical image of a sintered NCT solid, pressed using a mould (inset) of the MIT logo. **f**, SAXS data of the sample in **e** demonstrating that the bcc ordering is preserved throughout the process. a.u., arbitrary units; **q**, X-ray scattering vector; $I(\mathbf{q})$, intensity of scattered X-rays. NCT designs for **c**–**f** are provided in the Methods.

but when a non-solvent of the polymer—for example, *n*-decane—is added to crystallized NCTs, the interparticle spacing decreases continuously while preserving bcc ordering, as determined by small-angle X-ray scattering (SAXS) analysis (Fig. 2a, Supplementary Fig. 4). Notably, the collapse of the polymer brushes is reversible, and a lattice can be cycled between good solvents and non-solvents—a process that involves a 78% volumetric compression and expansion of the lattice—while maintaining crystallinity (Supplementary Fig. 5). As a result, alterations to the particle size, the length of the polymer chains that comprise the brush, and the solvent content can all be used to tune the distance between particles in a lattice across a broad range (4.1–21 nm; Supplementary Fig. 6).

Because solvent ceases to be a major volumetric component of the NCT lattice after the polymer brushes are condensed, the lattices can be subsequently dried without a loss of crystallinity, which enables characterization of their mesoscopic shapes (Fig. 2a, Supplementary Fig. 4). Scanning electron microscopy (SEM) micrographs of these dried lattices show that, under standard assembly conditions, they form faceted rhombic dodecahedral crystallites; rhombic dodecahedra are the thermodynamically favoured Wulff constructions for bcc lattices[15] (Fig. 1c). SEM imaging of cross-sections obtained by focused ion-beam milling further confirms that the materials are crystalline throughout the entire polyhedra (Fig. 1c).

Controlling NCT crystallite size

The faceted crystallites form quite rapidly, because the assembly process is guided by multiple weak supramolecular interactions that prevent the formation of kinetically trapped states[27]. As such, single-crystal architectures can be observed even with cooling rates 100 times faster than those required in similar nanoparticle-assembly methods[15,16]. Even when cooling as quickly as could be steadily controlled and measured (1 s per 0.1 °C; 5 min total annealing time), NCTs still formed single crystals (Supplementary Figs. 7, 8), and 15 s per 0.1 °C (around 1.25 h annealing time) was sufficient to generate faceted polyhedra (Supplementary Fig. 9).

Because the grain size of the crystallites is a key aspect of the microstructure of a material, complete structure control in macroscopic solids built from these assemblies requires methods to manipulate the crystallite diameter. Given the wide range of assembly conditions that yield single crystals (Fig. 2b, Supplementary Fig. 7), we postulated that it would be possible to tailor crystallite size as a function of these variables (Fig. 2b, c, Supplementary Figs. 8–26, Supplementary Table 3). By adjusting the concentration of the NCTs and the rate at which they are cooled, the diameter of the dried NCT crystallites could be tuned between about 500 nm and 30 µm. Additionally, the relationship between NCT concentration, annealing rate and final crystallite size

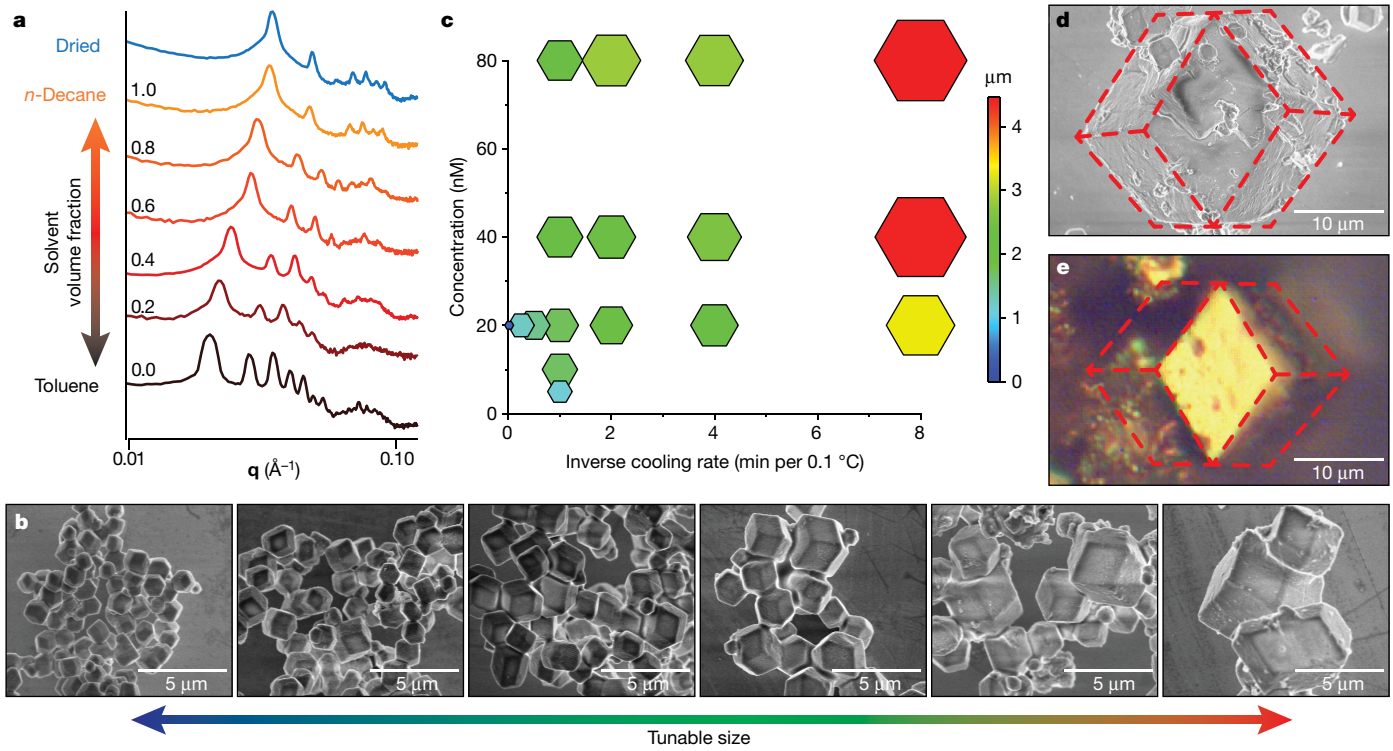

Fig. 2 | The formation of solid-state NCT superlattice polyhedra of controlled sizes. a, SAXS data for NCT crystallites in varying ratios of solvent (toluene) to non-solvent (*n*-decane) demonstrate a 40% swelling and deswelling of the lattice parameter, confirming that bcc ordering is maintained under all solvent conditions, including complete drying of the lattice. **b**, SEM micrographs of tunable crystallite size distributions achieved via slow-cooling NCTs (20 nM) at 0.25, 0.5, 1, 2, 4 and 8 min per 0.1 °C (left to right). **c**, Graph of median characteristic length as a function of inverse cooling rate and NCT concentration during crystallization, demonstrating that larger crystallites form at higher concentrations and slower cooling rates. Both the colour of the data point and its relative size correspond to median crystallite length; full statistical analysis is given in the Supplementary Information. **d**, **e**, SEM micrograph (**d**) and optical images (**e**) of the largest (>30 μm) NCT Wulff polyhedra formed at a concentration of 80 nM and an inverse cooling rate of 8 min per 0.1 °C. Lines have been added for reference.

can be explained by a mathematical model, which enables the average crystallite size to be reproducibly controlled, even up to sizes that are sufficient to be observed under a low-magnification optical microscope (see Methods for model details, and Supplementary Figs. 29–31).

Sintering NCT crystallites into macroscopic solids

Inspired by the sintering of nanocrystalline powders to produce macroscopic compacts of conventional metallic, ceramic and polymeric materials, we hypothesized that an analogous process could create larger NCT solids by using these crystallites as higher-order building blocks with inherent microstructural information (that is, crystallite size). In atomic materials, the application of high heat and pressure weakens bonding interactions, enabling powder particles to plastically flow and densify into a continuous structure[28,29]. Similar effects can be induced in NCT sintering; however, owing to the dynamic hydrogen bonds that link NCTs, only mild heating and pressure—centrifuging crystallites at 20,000*g* for 10 min at around 25 °C, collapsing the brush, and drying—are required to produce free-standing monolithic solids (Supplementary Fig. 34).

SAXS analysis confirms that the NCTs maintain their crystallinity throughout this processing, which indicates that the macroscopic deformation and 'sintering' was enabled by NCT reorganization rather than resulting simply from deformation of the polymer brush (Fig. 1f). Additionally, SEM imaging of cross-sections obtained by focused ion-beam milling revealed a densified structure with grain-boundary-like features (Figs. 1d, 3a, b), not unlike the microstructure of polycrystalline bulk solids. Densification is therefore proposed to occur via ordered reorganization of NCTs during sintering and crystallite deformation, which is supported by the observation of necking behaviour in the final solids (Fig. 3a, Supplementary Fig. 40). For example, cross-sections show adjacent sintered grains aligned at different angles (Fig. 3b); closer to the interface between these grains, the planes are slightly distorted via lattice strain as they try to form a low-energy grain boundary (Fig. 3c, d). At the inflection point of the change in angle of the planes, several dislocations can be observed, implying that the NCTs participate in energy-minimizing reorganization of particle positions during sintering. The lattice strains to allow each NCT to maximize hydrogen-bonding interactions with neighbouring particles, and dislocations form to accommodate excessive strain. The use of dynamic bonding interactions between neighbouring particles enables this crystal reorganization, and is the key design feature that gives rise to the ability of NCTs to 'sinter' into bulk materials without loss of crystallinity.

Analogous to methods to control grain sizes in conventional powder sintering, we predicted that the grain size of NCT compacts could also be tuned by appropriate selection of the diameter of the NCT crystallite precursors (Fig. 3). Two batches of NCT crystallites were therefore prepared using different cooling rates (15 s per 0.1 °C and 4 min per 0.1 °C) to generate two distinct populations of Wulff polyhedra sizes, and were sintered into separate macroscopic aggregates. SEM analysis of cross-sections of the resulting sintered solids reveals that the size distributions of crystallites before sintering do indeed correspond to the grain size within a sintered solid (with a slight reduction in grain size due to crystallite deformation and measurement artefacts) (Fig. 3, Supplementary Figs. 35–37). Notably, solids prepared from NCTs with larger size distributions were also qualitatively observed to have an increase in void space, which is consistent with a sintering mechanism[29] (Supplementary Fig. 35).

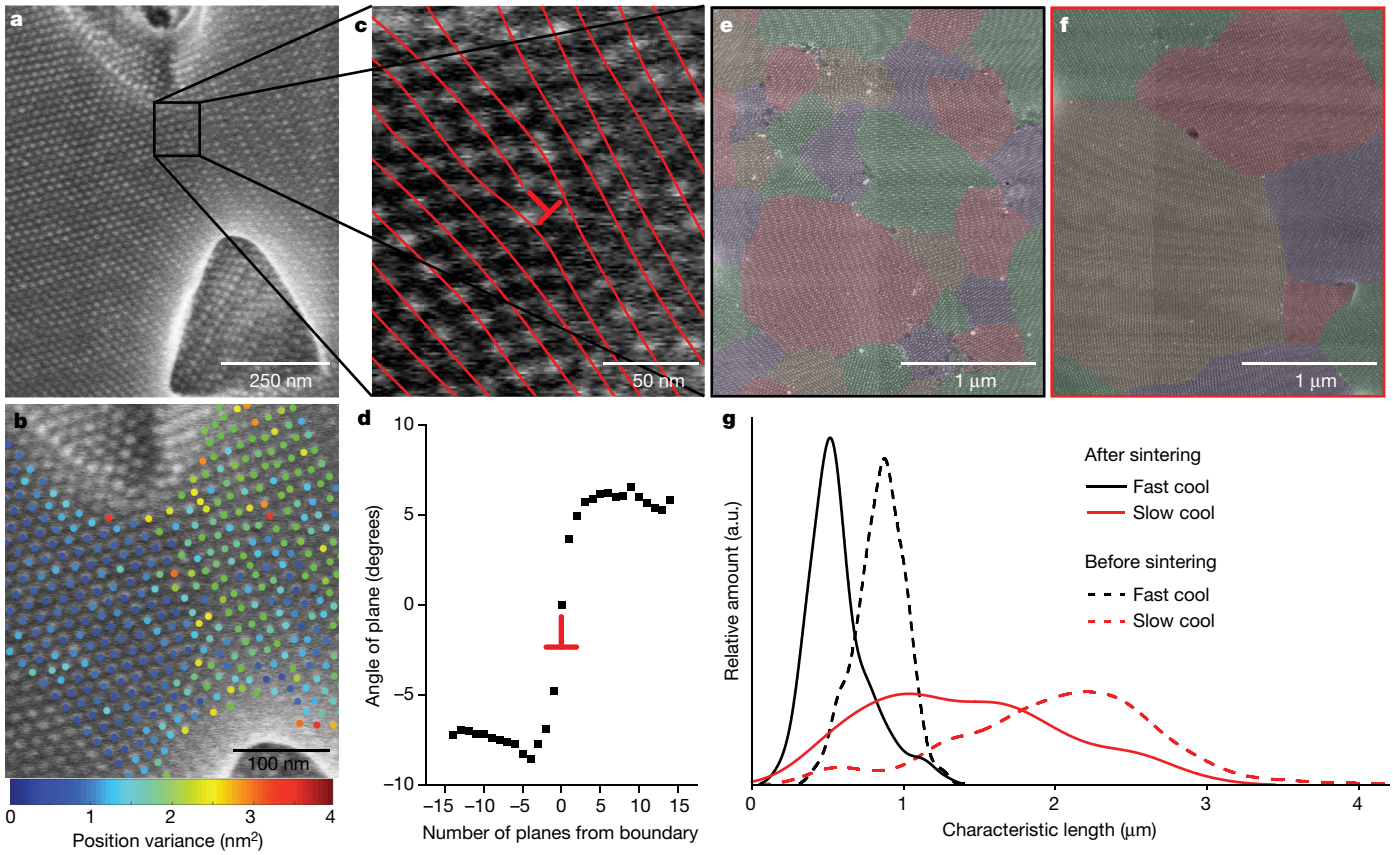

Fig. 3 | Control over microstructure in sintered NCT solids. a, SEM micrographs of the cross-section of a neck between two sintered NCT polyhedra. **b**, Positional variance of the particles overlaid onto the neck shown in **a**, confirming the presence of two distinct grains. **c**, Magnified view of the neck in **a**, with the crystallographic planes and a dislocation highlighted. **d**, The angle of the planes relative to the grain boundary in the neck region, indicating the offset between crystallites and the strain in the neck. **e**, **f**, SEM micrographs of cross-sections of sintered solids made from fast-cooled (15 s per 0.1 °C) (**e**) and slow-cooled (4 min per 0.1 °C) (**f**) NCT crystallites, demonstrating that the grain size of the crystallites is programmable. Each grain is coloured for reference. **g**, Size distribution of NCT crystallites (before sintering) and grains (after sintering) for both fast and slow cooling conditions, demonstrating that grain microstructure is dictated by initial crystallite size.

The ability to tune the microstructural features of these NCT solids suggests that they might also exhibit similar deformation mechanisms to atomic crystals; observation of these effects would strengthen the analogies drawn between the processing of atomic and NCT macroscopic solids[30]. To investigate this hypothesis, NCT lattices were sintered and dried, then subjected to 0.4 tonnes or 10 tonnes of mechanical force. Analysis of cross-sections by SEM (Supplementary Figs. 45–51) revealed that short-range ordering is largely preserved after pressing, but SAXS analysis indicates that long-range ordering is disturbed upon the application of increasing amounts of force (Supplementary Fig. 51). Applying a load of 0.4 tonnes to these materials notably decreases the amount of void space, and the grain boundaries appear to have a larger number of dislocations than an unpressed sample (Fig. 1d, Supplementary Figs. 36–41). At 10 tonnes, defects at the grain boundaries appear to be even more prominent. Furthermore, within the grains, the lattices appear distorted—we propose that this is due to plastic deformation of the NCT lattices and is responsible for the loss of ordering observed in SAXS. Additional features analogous to those observed in mechanically deformed atomic materials—such as fracture planes, twinning and paracrystalline distortion—are also readily evident (Supplementary Figs. 46–49).

Control of compositional heterogeneity

Previous work has demonstrated that NCTs can be synthesized with both gold (Au-NCTs) and iron oxide (IO-NCTs) nanoparticle cores[31]; the composition of the core does not alter the capacity of the NCTs to order into crystalline superlattices. Here, the assembly of faceted supracrystals and subsequent processing into bulk solids were also found to be largely unaffected by the identity of the nanoparticle core (Fig. 4, Supplementary Figs. 32, 33). Therefore, the sintering of solids with more complex hierarchical organization could in principle be achieved by assembling multi-component materials in which gold and iron oxide particles are distributed throughout the solid in either a homogeneous or heterogeneous manner.

Sintered NCT solids with distinct grains containing different nanoparticle compositions were prepared using a mechanically blended combination of bcc IO-NCT crystallites and bcc Au-NCT crystallites (Fig. 4b, g, Supplementary Fig. 38). The Au-NCTs and IO-NCTs remain phase-segregated in this sample, suggesting that minimal grain boundary diffusion occurs during sintering (Supplementary Fig. 41); the resulting heterogeneous microstructure is controlled by the relative amounts and sizes of the Au-NCT and IO-NCT crystallites used. Macroscopically observable heterogeneity can also be achieved by sintering together batches of Au-NCT and IO-NCT crystallites in a stepwise manner (Fig. 4i). By contrast, microscopically homogenous composites can be generated by synthesizing caesium chloride (CsCl)-type NCT crystallites formed from complementary DAP-functionalized Au-NCTs and Thy-functionalized IO-NCTs (Fig. 4c). In these CsCl-type lattices, each unit cell contains exactly one Au-NCT and one IO-NCT, but the overall crystallites form the same Wulff polyhedra as observed when only one particle composition is used (Supplementary Fig. 32). When CsCl-type crystallites are sintered, the result is a continuous macroscopic solid

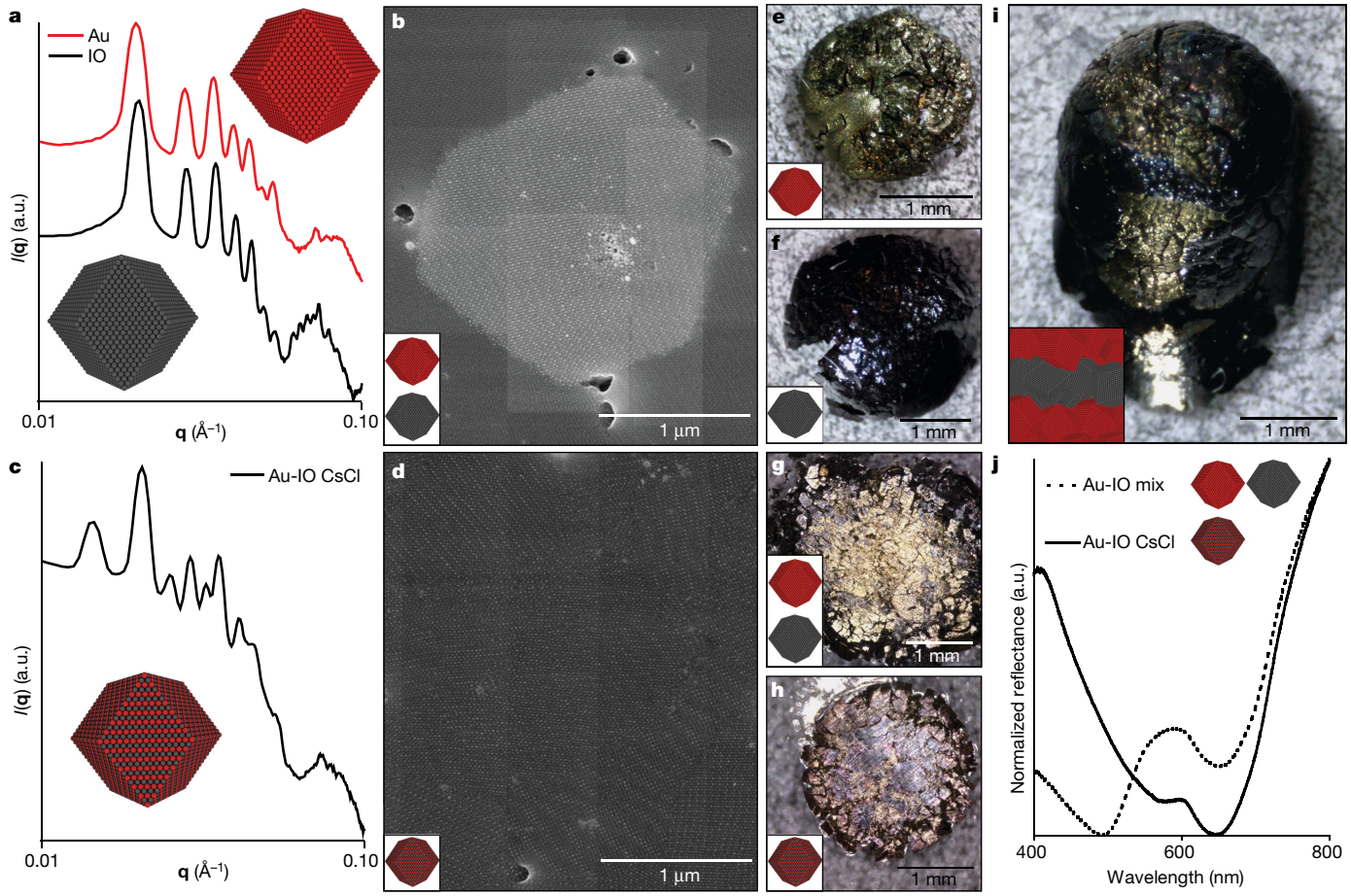

Fig. 4 | Independent control of the NCT solid composition, nanoscale ordering and microstructure. a, SAXS analysis of Au-NCT and IO-NCT crystallites in solution, demonstrating identical bcc ordering regardless of nanoparticle composition. **b**, SEM micrographs of a cross-section of a solid sintered from a blend of Au-NCT crystallites and IO-NCT crystallites, demonstrating a heterogeneous microstructure with neighbouring grains of distinct composition. **c**, SAXS data of co-assembled, complementary Au-NCTs and IO-NCTs demonstrating a CsCl-type lattice (Au and IO NPs were coated with DAP- and Thy-terminated polymers, respectively, ensuring CsCl ordering). **d**, SEM micrographs of a cross-section of a bulk solid sintered from CsCl-type NCT crystallites demonstrating a homogeneous microstructure in which each alternating nanoparticle is Au or IO. **e**–**h**, Optical images of the macroscopic, free-standing NCT solids fabricated from Au-NCTs (**e**), IO-NCTs (**f**), mechanically blended Au/IO-NCTs (**g**), and CsCl Au/IO-NCTs (**h**), pressed into solids with flat surfaces to enable optical characterization. **i**, The heterogeneous structure of successively sintered IO-Au-IO NCTs. **j**, Reflectance measurements of NCT solids, demonstrating that the microstructure of the material affects the bulk material properties. Au-NCT bcc lattices and the mechanically blended Au/IO NCT sample exhibit a metallic reflection peak at around 550 nm, which is absent in the CsCl sample.

with well defined, microscale grain sizes in which every other nanoparticle has a different composition (Fig. 4d, h, Supplementary Fig. 39). Taken together, these three types of structure demonstrate the ability to maintain a constant material composition, but introduce heterogeneity at the nano, micro and macroscopic length scales.

Controlling the structure across these size regimes can tailor the properties of self-assembled nanomaterials by dictating coupled interactions between particles. As an example, marked differences in the optical behaviour of these sintered solids are observed owing to different extents of AuNP plasmon coupling. Both the exclusively Au-NCT solid and the solid consisting of blended Au-NCT and IO-NCT bcc crystallites show a metallic reflectance at around 550 nm, which is attributed to strong plasmon coupling between AuNPs as a result of the small interparticle spacings. However, this peak is suppressed in CsCl lattices owing to the presence of the IO-NCT spacers between gold particles, which weakens the plasmon coupling between Au-NCTs (Fig. 4j).

Manipulation of the NCT solid macroscopic form

Because the components of IO-NCTs—that is, iron oxide nanoparticles and polystyrene polymers—can be readily synthesized in gram-scale quantities, and because NCT crystals can be sintered into bulk solids, it should also be possible to manipulate the macroscopic form of these structures with additional processing steps. To demonstrate this additional level of structural control, a sintered solid of IO-NCTs was prepared by the abovementioned centrifugation method (Fig. 4f, Supplementary Fig. 42), and gently pressed (about 0.05 tonnes) into a laser-cut polyoxymethylene mould of the Massachusetts Institute of Technology school logo. Removing the continuous NCT solid from the mould yielded a freestanding block in which the embossed logo was clearly visible (overall block dimensions of 3.9 mm × 2.6 mm × 0.25 mm) (Fig. 1e, Supplementary Fig. 44). SAXS analysis confirmed that the NCTs remained ordered after pressing (Fig. 1f), and SEM imaging revealed that the microstructure is similarly preserved (Supplementary Fig. 43). It is therefore possible to control the material structure of NCT-based composites—including the nanoparticle composition, superlattice ordering, polycrystalline microstructure and overall macroscopic form of the fabricated object—across seven orders of magnitude on the length scale.

Here we have demonstrated a method for the manufacture of bulk, solid materials from a nanoparticle-based building block that can be manipulated into arbitrary macroscopic shapes while maintaining

nanoscale control over ordering. Because there are many observable analogies between the processing of NCTs and of traditional bulk materials, these structures provide a tool with which to explore basic questions in processing science. For example, the nanoscale size of the NCT building blocks enables their in situ characterization (using electron microscopy) during assembly, sintering, or deformation to enable visualization of defect formation in a manner that would be challenging or impossible for atomic lattices. Furthermore, because the NCT assembly and sintering processes are not inherently tied to any specific nanoparticle composition, sintered NCT solids potentially allow for carefully calibrated interactions between nanoparticles—such as plasmonic coupling, controlled photoluminescence or magnonic bandgaps—to be incorporated into bulk solids for application in sensing, display or energy technologies[1,2,5,6]. The ability to fabricate hierarchically ordered, free-standing macroscopic structures with predetermined composition, nanoscale ordering and microstructure represents a major advancement for the field of nanomaterials synthesis and will enable further research into materials synthesis and structure–property relationships.

Online content

Any methods, additional references, Nature Research reporting summaries, source data, extended data, supplementary information, acknowledgements, peer review information; details of author contributions and competing interests; and statements of data and code availability are available at https://doi.org/10.1038/s41586-021-03355-z.

1. Begley, M. R., Gianola, D. S. & Ray, T. R. Bridging functional nanocomposites to robust macroscale devices. *Science* **364**, eaav4299 (2019).
2. Boles, M. A., Engel, M. & Talapin, D. V. Self-assembly of colloidal nanocrystals: from intricate structures to functional materials. *Chem. Rev.* **116**, 11220–11289 (2016).
3. Grzelczak, M., Liz-Marzán, L. M. & Klajn, R. Stimuli-responsive self-assembly of nanoparticles. *Chem. Soc. Rev.* **48**, 1342–1361 (2019).
4. Gabrys, P. A., Zornberg, L. Z. & Macfarlane, R. J. Programmable atom equivalents: atomic crystallization as a framework for synthesizing nanoparticle superlattices. *Small* **15**, 1805424 (2019).
5. Talapin, D. V., Lee, J.-S., Kovalenko, M. V. & Shevchenko, E. V. Prospects of colloidal nanocrystals for electronic and optoelectronic applications. *Chem. Rev.* **110**, 389–458 (2010).
6. Dreyer, A. et al. Organically linked iron oxide nanoparticle supercrystals with exceptional isotropic mechanical properties. *Nat. Mater.* **15**, 522–528 (2016).
7. Tan, A. T. L., Beroz, J., Kolle, M. & Hart, A. J. Direct-Write Freeform Colloidal Assembly. *Adv. Mater.* **30**, 1803620 (2018).
8. Hatton, B., Mishchenko, L., Davis, S., Sandhage, K. H. & Aizenberg, J. Assembly of large-area, highly ordered, crack-free inverse opal films. *Proc. Natl Acad. Sci. USA* **107**, 10354–10359 (2010).
9. Mirkin, C. A., Letsinger, R. L., Mucic, R. C. & Storhoff, J. J. A DNA-based method for rationally assembling nanoparticles into macroscopic materials. *Nature* **382**, 607–609 (1996).
10. Singh, G. et al. Self-assembly of magnetite nanocubes into helical superstructures. *Science* **345**, 1149–1153 (2014).
11. Vial, S., Nykypanchuk, D., Yager, K. G., Tkachenko, A. V. & Gang, O. Linear mesostructures in DNA–nanorod self-assembly. *ACS Nano* **7**, 5437–5445 (2013).
12. Gabrys, P. A. & Macfarlane, R. J. Controlling crystal texture in programmable atom equivalent thin films. *ACS Nano* **13**, 8452–8460 (2019).
13. Dong, A., Chen, J., Vora, P. M., Kikkawa, J. M. & Murray, C. B. Binary nanocrystal superlattice membranes self-assembled at the liquid-air interface. *Nature* **466**, 474–477 (2010).
14. Ye, X. et al. Structural diversity in binary superlattices self-assembled from polymer-grafted nanocrystals. *Nat. Commun.* **6**, 10052 (2015).
15. Auyeung, E. et al. DNA-mediated nanoparticle crystallization into Wulff polyhedra. *Nature* **505**, 73–77 (2014).
16. Kang, Y. et al. Heterogeneous catalysts need not be so "heterogeneous": monodisperse Pt nanocrystals by combining shape-controlled synthesis and purification by colloidal recrystallization. *J. Am. Chem. Soc.* **135**, 2741–2747 (2013).
17. de Nijs, B. et al. Entropy-driven formation of large icosahedral colloidal clusters by spherical confinement. *Nat. Mater.* **14**, 56–60 (2015).
18. Lewis, D. J., Zornberg, L. Z., Carter, D. J. D. & Macfarlane, R. J. Single-crystal Winterbottom constructions of nanoparticle superlattices. *Nat. Mater.* **19**, 719–724 (2020).
19. Nagaoka, Y. et al. Superstructures generated from truncated tetrahedral quantum dots. *Nature* **561**, 378–382 (2018).
20. Jiang, W. et al. Emergence of complexity in hierarchically organized chiral particles. *Science* **368**, 642–648 (2020).
21. Hueckel, T., Hocky, G. M., Palacci, J. & Sacanna, S. Ionic solids from common colloids. *Nature* **580**, 487–490 (2020).
22. Zhang, J. et al. Self-assembling nanocomposite tectons. *J. Am. Chem. Soc.* **138**, 16228–16231 (2016).
23. Santos, P. J., Cheung, T. C. & Macfarlane, R. J. assembling ordered crystals with disperse building blocks. *Nano Lett.* **19**, 5774–5780 (2019).
24. Auyeung, E., Macfarlane, R. J., Choi, C. H. J., Cutler, J. I. & Mirkin, C. A. Transitioning DNA-engineered nanoparticle superlattices from solution to the solid state. *Adv. Mater.* **24**, 5181–5186 (2012).
25. Lee, S., Zheng, C. Y., Bujold, K. E. & Mirkin, C. A. A cross-linking approach to stabilizing stimuli-responsive colloidal crystals engineered with DNA. *J. Am. Chem. Soc.* **141**, 11827–11831 (2019).
26. Birshtein, T. M. & Lyatskaya, Yu. V. Theory of the collapse-stretching transition of a polymer brush in a mixed solvent. *Macromolecules* **27**, 1256–1266 (1994).
27. Santos, P. J., Cao, Z., Zhang, J., Alexander-Katz, A. & Macfarlane, R. J. Dictating nanoparticle assembly via systems-level control of molecular multivalency. *J. Am. Chem. Soc.* **141**, 14624–14632 (2019).
28. Chaim, R., Levin, M., Shlayer, A. & Estournes, C. Sintering and densification of nanocrystalline ceramic oxide powders: a review. *Adv. Appl. Ceramics* **107**, 159–169 (2008).
29. Olevsky, E. A. Theory of sintering: from discrete to continuum. *Mater. Sci. Eng. Rep.* **23**, 41–100 (1998).
30. Schall, P., Cohen, I., Weitz, D. A. & Spaepen, F. Visualizing dislocation nucleation by indenting colloidal crystals. *Nature* **440**, 319–323 (2006).
31. Santos, P. J. & Macfarlane, R. J. Reinforcing supramolecular bonding with magnetic dipole interactions to assemble dynamic nanoparticle superlattices. *J. Am. Chem. Soc.* **142**, 1170–1174 (2020).

Methods

Materials, instrumentation and characterization methods

Materials. 2,6-Diaminopyridine, thymine, acetyl chloride, 11-bromoundecan-1-ol, sodium azide, EDTA sodium salt, 2-bromoisobutyryl bromide, styrene, *N*,*N*,*N*′,*N*″,*N*‴-pentamethyldiethylenetriamine (PMDETA), propargyl alcohol and citric acid monohydrate were purchased from Acros. Trisodium citrate dihydrate, hexamethyldisilazane, tris[2-(dimethylamino)ethyl]amine (Me_6TREN) and tin(II) 2-ethylhexanoate were purchased from Alfa Aesar. Docosane, phosphorous acid, cyclohexamine, ferric chloride hexahydrate, oleic acid, copper(I) bromide, hydrochloric acid and copper(II) bromide were purchased from Sigma Aldrich. *n*-Hexane, *n*-octane, *n*-decane and gold(III) chloride trihydrate were purchased from Beantown Chemical. Aminoethanethiol and sodium oleate were purchased from TCI America. Basic alumina and general solvents were purchased from Fisher Scientific. A polyoxymethylene bar was purchased from McMaster Carr. All chemicals—including solvents—were used without further purification, except for styrene, which was passed through a short column of basic alumina to remove inhibitor before polymerization.

Instrumentation. Centrifugation was performed with an Eppendorf 5424 centrifuge. Gel permeation chromatography (GPC) characterization was performed on an Agilent Technologies Infinity 1260 GPC system with triple detection (refractive index, 90° light scattering, and viscometry), with Resipore columns, and with tetrahydrofuran (THF) as the eluent at 1.0 ml min^{-1}. Ultraviolet–visible absorption spectra and measurements were obtained on a Cary-5000 spectrometer. SAXS measurements were performed at the Massachusetts Institute of Technology (MIT) Center for Materials Science and Engineering (CMSE) X-ray Diffraction Shared Experimental Facility on a SAXSLAB system. The Rigaku 002 microfocus X-ray source produced Cu Kα1 X-rays of wavelength 1.5409 Å; Osmic staggered parabolic multilayer optics focused the beam crossover at the second pinhole. Two sets of JJ X-ray jaw collimation slits set at 0.45 mm and 0.2 mm, respectively, were used to define the beam. The system was calibrated using silver behenate as a standard. Solvated SAXS samples were loaded into a short section of 1.5-mm diameter polyimide tubing (Cole-Parmer) and sealed at both ends with epoxy. Before loading samples into the tubing, one end was sealed with epoxy and the tubing was baked at 110 °C overnight. Dried SAXS samples were prepared by casting onto polyimide film, or for macroscopic samples by wrapping in polyimide tape. The lowest q peak identified in SAXS (q_0) was fit using a pseudo-Voight function, and the interparticle distance d for bcc crystals was determined as:

$$d_{bcc} = \frac{\pi\sqrt{6}}{q_0} \quad (1)$$

and for CsCl crystals as:

$$d_{CsCl} = \frac{\pi\sqrt{3}}{q_0}. \quad (2)$$

Transmission electron microscopy (TEM) was performed with a JEOL 2010 Advanced High-Performance transmission electron microscope, with samples cast onto formvar-coated TEM grids (Ted Pella). Top-down SEM was performed on either a Zeiss Sigma 300 VP Field Emission scanning electron microscope (5 kV electron beam with in-lens detector) or a Helios Nanolab 600 dual beam instrument (86 pA and 5 kV electron beam with in-lens detector). To be imaged, samples were cast and dried onto copper tape or silicon wafers (150 mm P-Type Prime (100) wafers with polished surfaces purchased from Wafernet) which had 2 nm of chromium (Cr) and 8 nm of gold (Au) deposited (via AJA eBeam evaporator) to aid conduction. Cross-sectional micrographs were collected on the Helios Nanolab 600 dual beam focused ion-beam milling system with a 52° relative difference between the ion and electron beam. After a layer of titanium was deposited over the area of interest, the sample was milled with a 93 pA (30 kV) ion beam. Each cross-section was imaged with an 86 pA (5 kV) electron beam using the in-lens detector on the scanning electron microscope without using the software's tilt correction. SEM images were stitched together using Photoshop and the y-axis scale was adjusted for tilt angle such that it is representative of the real space length using the following equation:

$$y_{processed} = \frac{y_{raw}}{\cos(90^\circ - 52^\circ)} = \frac{y_{raw}}{\cos(38^\circ)} = 1.269 \times y_{raw}. \quad (3)$$

Reflectance data of NCT solids were obtained on a Cary 5000 instrument. NCT samples were placed on a glass slide and mechanically flattened. Data was collected at a rate of 100 nm min^{-1} at intervals of 0.167 nm, with a spectral bandwidth of 2 nm. Raw reflection data were weighted against reflection data using a silicon wafer mirror. To compare reflection spectra between samples of variable size and roughness, the data was normalized after weighting.

Synthesis of NCTs

The synthesis of the DAP initiator, the Thy initiator and the phosphonate anchor have been previously reported[31].

The DAP polymers were synthesized by the activator regenerated by electron transfer atom transfer radical polymerization (ARGET-ATRP)[32] of polystyrene using the DAP initiator as previously reported[23]. The Thy polymers were synthesized by the ATRP of polystyrene using the Thy initiator as previously reported[22]. GPC traces of the polymers used in this work can be found in Supplementary Fig. 1, and the results are summarized in Supplementary Table 1.

After polymerization, the terminal bromine atom of polymers that were to functionalize gold nanoparticles was substituted with aminoethanethiol, as described previously[22]. The terminal bromine of polymers that were to functionalize iron oxide nanoparticles was substituted with sodium azide, and a 'click' reaction was performed to install the phosphonate anchor as described previously[31].

Citrate-capped gold nanoparticles were synthesized by a literature procedure[33] that was slightly modified[27]. Iron oxide nanoparticles were synthesized according to a literature procedure from the thermal decomposition of an iron oleate precursor[31,34]. TEM micrographs of the nanoparticles used in this work can be found in Supplementary Fig. 2, and their sizes and distributions are summarized in Supplementary Table 2.

Au-NCTs were synthesized as previously reported[22]. In brief, a solution of as-synthesized gold nanoparticles was added to an equal volume of 1 mg ml^{-1} thiolated DAP or Thy polystyrene, and was vigorously shaken for 1 min. The resulting pink precipitate was collected by gentle centrifugation and redispersed in *N*,*N*-dimethylformamide (DMF). The NCTs were then subjected to a series of three centrifuge cycles (5,000*g*, 45 min), redispersing in DMF, toluene, and toluene. The concentration of the NCTs was measured using Beer's Law, and adjusted to match the desired concentration for the experiment.

IO-NCTs were synthesized as previously described[31]. In brief, iron oxide nanoparticle docosane reaction mixture (500 mg) was dissolved in 4 ml THF. Reaction byproducts were removed by centrifugation (2 × 8,500*g*) and redispersion in THF. The suspension of nanoparticles in THF was divided in half, and added to either DAP or Thy polymer equipped with the phosphonate anchor (40 mg). The solutions were shaken overnight, and then purified by three centrifuge cycles (8,500*g*), redispersing in THF, toluene and toluene.

NCT crystallization

To prepare crystalline Au-NCT assemblies, equal volumes of purified DAP and Thy NCTs were combined in a PCR tube. Analysis of the melting curve (Supplementary Fig. 28) indicated that the standard NCTs

(15 nm Au NPs with 14 kDa polymer) were totally dissociated at 55 °C. Therefore, the annealing process was performed by slow-cooling the mixed NCT solution from 55 °C to 25 °C in a Techne Prime Thermal Cycler at a desired rate (inverse cooling rate of 1 min per 0.1 °C unless otherwise stated). IO-NCTs were crystallized by heating to 80 °C on a heat block, removing the sample, and allowing the NCTs to return to room temperature.

Collapsing the polymer brush

NCTs cast directly from toluene do not retain their ordering upon solvent evaporation (Supplementary Fig. 3). As the solvent evaporates, the polymer brush uncontrollably deswells and capillary forces distort the lattice, although some local ordering is maintained.

Ordering can be preserved by gradually adding a poor solvent that does not disrupt the hydrogen-bonding interactions of the NCTs (Supplementary Fig. 4). *n*-Decane was the preferred solvent for the experiments because its slower evaporation rate allowed for trace amounts of residual toluene to be removed before the assembly completely dried. The typical procedure was to increase the volume fraction of non-solvent by 0.2 every 30 min, and when the solution reached 80% non-solvent it was removed with a needle and replaced with pure non-solvent. The system could accommodate faster addition rates, but shaking samples to mix the solvents would frequently generate static electricity, which would pull the NCTs out of solution and destroy them, making their study difficult. Therefore, a more conservative procedure that allowed ample time for solvent diffusion was preferred.

Additionally, the collapsed NCT brush can be swollen with toluene again, without any loss in ordering (Supplementary Fig. 5).

A potential key advantage of these NCT solids with collapsed polymer brushes is the ability to assemble lattices of nanoparticles with very small interparticle distances, which could find use in plasmonic, optical, or magnetic materials[35,36]. To demonstrate this, Au-NCTs were assembled with a 6 kDa polymer brush and collapsed, leading to well-ordered lattices with an interparticle distance of 19.5 nm, or a surface-to-surface distance of 4.1 nm (Supplementary Fig. 6).

Controlling NCT crystallite size with cooling rate, concentration

To investigate the effects of NCT concentration and the cooling rate on crystallite size, several samples were crystallized via slow-cooling as described in the section 'NCT Crystallization' with various inverse cooling rates (1 s per 0.1 °C to 8 min per 0.1 °C) and NCT concentrations (5 nM to 80 nM). After each of these samples were analysed to demonstrate that each was crystalline (key SAXS data collected in Supplementary Fig. 7), the resulting crystallites were collected and their polymer brushes collapsed, and they were then drop-cast onto substrates for SEM analysis. A minimum of 50 micrographs for each condition were collected, in which each micrograph contained several crystallites, which tend to conglomerate together on the substrate. Three characteristic, representative SEM micrographs of each condition are included for reference in Supplementary Figs. 8–24. The individual crystallites in each micrograph were measured in ImageJ by tracing the dimensions with a stylus and averaging the major and minor axis lengths to yield a characteristic length (roughly akin to a diameter). The number of crystallites (N) measured for each condition is summarized in Supplementary Table 3 and included at minimum 200 individual crystallites. Histograms of characteristic length reveal roughly Gaussian size distributions for every condition (Supplementary Figs. 8–26), with increasing average values for slower cooling rates and higher concentrations. Descriptive statistics of each distribution are summarized in Supplementary Table 3.

Upon determining that the 80 nM, 8 min per 0.1 °C condition yielded crystallites with the largest average size, the sample was searched for its largest crystallites. These crystallites were not included in the size analysis, which consisted of randomly selected regions to image; however, the SEM micrographs of the largest three observed crystallites are included in Supplementary Fig. 27 for reference.

Mathematical model of NCT crystallization

Traditional crystallization theory would predict that the size of NCT crystallites is positively correlated with a slower cooling process and inversely correlated with precursor concentration, owing to suppression of the nucleation rate[37]. The expected relationship with cooling rate is observed; however, higher precursor concentrations yield larger crystallites with a broader distribution of sizes. To understand this unexpected result, a model was developed that treats the cooling NCTs as clusters that collapse into an aggregate, the size of which is determined by the number of particles in a diffusion-limited volume as the system crystallizes[38,39]. The model (see Supplementary Materials for derivation and further discussion) predicts a cluster size, N:

$$N = cV = \frac{4}{3}\pi W^{3/2} D^{3/2} \times c\tau^{3/2}, \tag{4}$$

where c is the total concentration of particles in solution and V is the volume of the diffusion-limited region. This volume is estimated for nanoparticles with diffusivity D, which melt in a finite window of temperature with range W, in which the particles 'collapse' while cooling at a reciprocal rate of τ.

Because the crystallite volume is a function of the number of particles in the crystallite, the 1D characteristic crystal size L then scales as:

$$L \approx N^{1/3} \approx c^{1/3}\tau^{1/2}. \tag{5}$$

This is consistent with the observed data for concentration and reciprocal rate (Supplementary Fig. 31).

Sintering NCTs

Crystallite preparation. The crystallites used in the sintering protocol to produce different grain sizes were synthesized via slow-cooling as described in the section 'NCT Crystallization'. The two protocols used were 15 s per 0.1 °C (fast cool) and 4 min per 0.1 °C (slow cool), both at 20 nM concentration, and resulted in crystallites that were almost identical to those shown in Supplementary Figs. 9 and 13, respectively. However, as a control, some of the crystallites from each batch were imaged by SEM and their size distribution was analysed in the manner as described in the section 'Controlling NCT crystallite size with cooling rate and concentration'. The measured size distributions (Fig. 3c) are therefore from the same batch of crystallites used to produce the sintered solids and are directly comparable to the measured distribution of grain sizes.

The mixes between Au-NCTs and IO-NCTs were prepared in the same fashion, with the IO-NCTs added to the Au-NCTs and mixed with a pipette before sintering. It should be noted that the concentration of IO-NCTs is considerably higher than that of Au-NCTs. Consequently, CsCl lattices formed slightly rounded shapes instead of polyhedra (Supplementary Fig. 32b, c), and the sintered solids were predominantly IO-NCTs (Supplementary Fig. 40). For the CsCl NCTs, the excess IO-NCTs were removed with a syringe before any further processing. SEM imaging of the crystallites used to make the sintered solids in the main text are presented in Supplementary Fig. 32. SAXS analysis demonstrates crystallinity regardless of composition and the presence of a CsCl crystallographic phase (Supplementary Fig. 33).

Sintering protocol. To sinter NCT crystallites into macroscopic solids, they were loaded into a microcentrifuge tube and centrifuged for 10 min at 20,000*g*. Other speeds were also effective, but resulted in a less dense microstructure. Moreover, the sintering process was only effective while the brush was in toluene, probably because new hydrogen bonds were slower to form in the collapsed state. After centrifuging the samples underwent the standard polymer-brush collapse, and were allowed to dry. The subsequent materials were then characterized by SEM (Supplementary Fig. 34) and by optical microscopy (Fig. 4e–h).

Cross-sections. The sintered solids were subsequently cross-sectioned mechanically with a razor blade followed by focused ion-beam milling (as described in the section 'Instrumentation') to image the interior microstructure (Supplementary Fig. 35). For each of the four sintering conditions, cross-sections of the products were analysed by SEM, stitched into one composite image in Photoshop, and adjusted for tilt via equation (3). Extended, large-area portions of the cross-section images collected are included in Supplementary Figs. 37–40; smaller sections are included in Figs. 3, 4.

For the two cross-sections demonstrating different grain sizes, individual grains within the cross-section were identified by eye and coloured in Photoshop. The grains were then outlined and analysed in ImageJ in the same manner as the pre-sintering crystallites. The average of the major and minor axis was used as the characteristic length of each grain and the distributions of sizes is shown in Fig. 3c. Note that the observed cross-section is a 2D slice of a 3D grain structure. Therefore, the size measured in cross-section is smaller than the true 3D size, but can be geometrically related[40] for comparison between pre- and post-sintering.

In the cross-sections containing both Au-NCTs and IO-NCTs, the composition of each nanoparticle can be determined from the SEM contrast. Au-NCTs, with high electron density, will appear brighter whereas IO-NCTs, with a lower electron density, will appear darker.

Evidence of a sintering mechanism and grain boundary diffusion. The experiments in this work did not provide conclusive evidence for grain-boundary diffusion during sintering, but experiments with blended IO-NCTs and Au-NCTs allowed for easy visualization of the interface between crystallites. In several regions, substantial distortions of the lattice were observed, suggesting some degree of grain-boundary diffusion may be possible under the correct processing conditions. For example, small segments of both IO-NCTs and/or Au-NCTs grains were observed to have deformed to match the orientation of neighbouring grains (Supplementary Fig. 41). Furthermore, lattice strain seems to orient the NCTs such that the lattices align at the interfaces. However, the large size of the NCTs as compared to atoms seems to make particle diffusion impossible.

Mechanically shaping NCTs

To mechanically shape the bulk NCT materials, a sintered solid was first prepared from IO-NCTs (16 nm IO-NPs and 8 kDa polymer) using the procedure described in the section 'Sintering Protocol', yielding a monolithic solid that was easily observed by eye and manipulated by hand (Supplementary Fig. 42). The sample was then placed into a polyoxymethylene mould that had been cut with a laser cutter (Fig. 1e, inset), and 0.05 tonnes was applied for 1 h. The result was a material with a macroscale, well defined embossed structure that was visible by eye (Fig. 1e). SEM analysis of the pressed sample revealed that crystallinity was maintained after processing (Supplementary Fig. 43). To demonstrate the robustness of this processing route, a similar sample was produced using IO-NCTs with 13 kDa polymers and mechanically processed in an identical fashion (Supplementary Fig. 44). Ordering (as demonstrated by SAXS analysis) was slightly less well maintained in this sample than in those prepared with a shorter polymer brush, probably because these 'softer' (higher inorganic fraction) NCTs are more capable of deforming during sintering.

Data availability

All data are available in the main Article and Supplementary Information, or from the corresponding author upon reasonable request.

32. Matyjaszewski, K. Atom transfer radical polymerization (ATRP): current status and future perspectives. *Macromolecules* **45**, 4015–4039 (2012).
33. Bastús, N. G., Comenge, J. & Puntes, V. Kinetically controlled seeded growth synthesis of citrate-stabilized gold nanoparticles of up to 200 nm: size focusing versus Ostwald ripening. *Langmuir* **27**, 11098–11105 (2011).
34. Park, J. et al. Ultra-large-scale syntheses of monodisperse nanocrystals. *Nat. Mater.* **3**, 891–895 (2004).
35. Huh, J.-H., Lee, J. & Lee, S. Soft plasmonic assemblies exhibiting unnaturally high refractive index. *Nano Lett.* **20**, 4768–4774 (2020).
36. Majetich, S. A., Wen, T. & Booth, R. A. Functional magnetic nanoparticle assemblies: formation, collective behavior, and future directions. *ACS Nano* **5**, 6081–6084 (2011).
37. De Yoreo, J. J. et al. Crystallization by particle attachment in synthetic, biogenic, and geologic environments. *Science* **349**, aaa6760 (2015).
38. Mirabello, G. et al. Crystallization by particle attachment is a colloidal assembly process. *Nat. Mater.* **19**, 391–396 (2020).
39. Ou, Z., Wang, Z., Luo, B., Luijten, E. & Chen, Q. Kinetic pathways of crystallization at the nanoscale. *Nat. Mater.* **19**, 450–455 (2019).
40. Depriester, D. & Kubler, R. Resolution of the Wicksell's equation by minimum distance estimation. *Image Anal. Stereol.* **38**, 213–226 (2019).

Acknowledgements This work was primarily supported by an NSF CAREER grant, award number CHE-1653289; supported in part by the US Army Research Office under grant W911NF-18-1-0197 and the Air Force Office of Scientific Research FA9550-17-1-0288; and made use of the MRSEC Shared Experimental Facilities at MIT, supported by the NSF under award DMR 14-19807. P.J.S., P.A.G. and L.Z.Z. acknowledge support from the NSF Graduate Research Fellowship Program under grant NSF 1122374.

Author contributions P.J.S. synthesized the materials, developed the processing methods, collected characterization data, designed the experiments and wrote the manuscript. P.A.G. developed characterization methods, collected microscopy data, designed the experiments and wrote the manuscript. L.Z.Z. developed the model and wrote the manuscript. M.S.L. collected characterization data and wrote the manuscript. R.J.M. designed the experiments and wrote the manuscript.

Competing interests The authors declare no competing interests.

Additional information

Supplementary information The online version contains supplementary material available at https://doi.org/10.1038/s41586-021-03355-z.

Correspondence and requests for materials should be addressed to R.J.M.

Peer review information *Nature* thanks the anonymous reviewers for their contribution to the peer review of this work.